

**Naval Surface Warfare Center
Carderock Division**

West Bethesda, MD 20817-5700

CRDKNSWC/HD-1362-07 May 1998

Hydromechanics Directorate

Research and Development Report

**Drag Calculations of Unappended Bodies of
Revolution**

By

Joseph J. Gorski

CRDKNSWC/HD-1362-07 Drag Calculations of Unappended Bodies of Revolution

19990305 001



Approved for Public Release, Distribution Unlimited

REPORT DOCUMENTATION PAGE

Form Approved
OMB No. 0704-0188

Public reporting burden for this collection of information is estimated to average 1 hour per response, including the time for reviewing instructions, searching existing data sources, gathering and maintaining the data needed, and completing and reviewing the collection of information. Send comments regarding this burden estimate or any other aspect of this collection of information, including suggestions for reducing this burden, to Washington Headquarters services, Directorate for Information Operations and Reports, 1215 Jefferson Davis Highway, Suite 1204, Arlington, VA 22202-4302, and to the Office of Management and Budget, Paperwork Reduction Project (0704-0188), Washington, DC 20503.

1. AGENCY USE ONLY (Leave blank)	2. REPORT DATE May 1998	3. REPORT TYPE AND DATES COVERED R & D Final	
4. TITLE AND SUBTITLE Drag Calculations of Unappended Bodies of Revolution		5. FUNDING NUMBERS PN: F2033 WU: 2630-707	
6. AUTHOR(S) Joseph J. Gorski		8. PERFORMING ORGANIZATION REPORT NUMBER CRDKNSWC/HD-1362-07	
7. PERFORMING ORGANIZATION NAME(S) AND ADDRESS(ES) Naval Surface Warfare Center Carderock Division 9500 MacArthur Boulevard West Bethesda, MD 20817-5700			
9. SPONSORING/MONITORING AGENCY NAME(S) AND ADDRESS(ES)		10. SPONSORING/MONITORING AGENCY REPORT NUMBER	
11. SUPPLEMENTARY NOTES			
12a. DISTRIBUTION/AVAILABILITY STATEMENT Approved for public release; distribution is unlimited.		12b. DISTRIBUTION CODE	
13. ABSTRACT (Maximum 200 words) This report describes efforts to compute drag forces on unappended bodies of revolution using the Reynolds averaged Navier-Stokes (RANS) equations. Calculations are performed for three different bodies of revolution with length to diameter ratios of 10, 8, and 5. Four different grids are used for each body with different point densities and clusterings which demonstrate solution dependency on the grids. The flows are computed over a Reynolds number range of 2.0 to 25.0 million, based on body length, and compared to data sets that were both tripped with sand and untripped.			
14. SUBJECT TERMS Navier-Stokes equations bodies of revolution turbulent transition		15. NUMBER OF PAGES 30	
		16. PRICE CODE	
17. SECURITY CLASSIFICATION OF REPORT UNCLASSIFIED	18. SECURITY CLASSIFICATION OF THIS PAGE UNCLASSIFIED	19. SECURITY CLASSIFICATION OF ABSTRACT UNCLASSIFIED	20. LIMITATION OF ABSTRACT SAR

CONTENTS

	Page
ABSTRACT	1
ADMINISTRATIVE INFORMATION	1
INTRODUCTION	1
SOLUTION TECHNIQUE	2
NUMERICAL RESULTS	3
Model 4159	4
Model 4158	13
Model 4155	14
CONCLUSIONS	24
ACKNOWLEDGMENTS	25
REFERENCES	27

FIGURES

	Page
1. Coarse grid for Model 4159.	5
2. Fine grid for Model 4159.	6
3. Y^+ for Model 4159 at a Reynolds number of 2.0×10^6	7
4. Law of the wall plots at $Re = 2.0 \times 10^6$	8
5. Y^+ for Model 4159 at a Reynolds number of 25.0×10^6	8
6. Law of the wall plots for grids C0 and F0 at $Re = 25.0 \times 10^6$	9
7. Law of the wall plots for grids C1 and F1 at $Re = 25.0 \times 10^6$	10
8. C_t for Model 4159.	10
9. C_F for Model 4159.	11
10. Skin friction comparisons for Model 4159.	12
11. C_r for Model 4159.	13
12. Surface pressure comparison for Model 4159.	14
13. Coarse grid for Model 4158.	15
14. Fine grid for Model 4158.	16
15. C_t for Model 4158.	17
16. C_F for Model 4158.	17
17. Skin friction comparison for Model 4158.	18
18. C_r for Model 4158.	18
19. Surface pressure comparison for Model 4158.	19
20. Coarse grid for Model 4155.	20
21. Fine grid for Model 4155.	21

22. C_t for Model 4155.	22
23. C_F for Model 4155.	22
24. Skin friction comparison for Model 4155.	23
25. C_r for Model 4155.	23
26. Surface pressure comparison for Model 4155.	24

ABSTRACT

This report describes efforts to compute drag forces on unappended bodies of revolution using the Reynolds averaged Navier-Stokes (RANS) equations. Calculations are performed for three different bodies of revolution with length to diameter ratios of 10, 8, and 5. Four different grids are used for each body with different point densities and clusterings which demonstrate solution dependency on the grids. The flows are computed over a Reynolds number range of 2.0×10^6 to 25.0×10^6 , based on body length, and compared to data sets that were both tripped with sand and untripped.

ADMINISTRATIVE INFORMATION

This work was primarily funded by the Advanced Submarine Research and Development Office (NAVSEA 92R) under the 6.4 Ship Design Tools Project (Project No. F2033), RANS Implementation Task, with internal Work Unit Number 1-2630-707-50. This project was also supported in part by the Carderock Division of the Naval Surface Warfare Center's In-house Laboratory Independent Research Program sponsored by the Office of Naval Research and administered by the Research Director, Code 0112, under Program Element 61152N with internal Work Unit Number 1-5400-600. The work described in this report was performed by the Propulsor Department of the Hydromechanics Directorate, Carderock Division, Naval Surface Warfare Center.

INTRODUCTION

There has been much effort in recent years to apply Reynolds Averaged Navier-Stokes (RANS) flow solvers to complex flow fields. The numerical results provide velocity and pressure descriptions around the entire configuration as well as force and moment predictions. Additionally, the computations provide complete "pictures" of flow fields by which complex fluid dynamics phenomena can be investigated in more detail than typically available with experiments. Computations can be used to minimize the amount of experimental testing needed, or they can be done simultaneously with testing to get a more complete description of the flow field. A huge potential area for RANS calculations is the study of Reynolds number effects, particularly as they pertain to full scale versus model scale.

Because RANS computations can be applied from model through to full scale there is a great deal of interest in determining how accurately such codes can predict changes in the flow field due to changes in the Reynolds number. There is nothing that inherently limits the RANS codes from being applied to different Reynolds numbers, but there are doubts as to their ability to predict full scale effects. At high Reynolds numbers the boundary layers are relatively thinner, based on body length, than what is found at model scale so grids need to be finer and more tightly packed near the wall. There

is then the question of whether or not grids can be made fine enough at full scale, because of the current precision of the computers, to resolve the sublayer flow. Due to lack of experimental data there is even the question, by some, whether the current turbulence models properly model the correct physics at full scale. Of course, there are also comparisons at model scale that are not satisfactory. One problem is that the model scale data with which the results from the codes are compared is either transitional or needs to be tripped to stimulate transition to fully turbulent flow. In some sense full scale calculations may be more straight forward than model scale computations as the flow should be fully turbulent.

One area where Reynolds number effects are particularly important is in the estimation of drag. The drag generated by a particular configuration is a dominant driver of the powering requirements of that configuration. The thrust of the propulsor must match the drag of the vehicle, including all appendages, for self propulsion. Consequently, there is a real need to predict the drag of various geometries accurately. Traditional flat plate friction equations are often inadequate for estimating drag due to pressure gradient and surface curvature effects. Various potential flow/boundary layer methods will generally provide a more accurate estimate, but such methods cannot be extended to complex fully appended geometries. Full RANS solvers are extendible to the configurations of interest. However, when using RANS solvers attention must be directed to properly gridding the entire domain as inadequate grid resolution will lead to poor predictions, even on bare bodies of revolution. To obtain force and moment data from a RANS code the computed pressure and stresses must be integrated over the body. Computing the correct pressure drag can be difficult on certain geometries as the net drag is a small value obtained by taking the difference of the two large opposing forces generated at the bow and stern.

In an effort to determine how well RANS codes can predict the drag of an unappended body of revolution the current study is undertaken. Resistance and powering measurements are usually done in the straight ahead condition and due to the relatively small appendages on a submarine the drag generated by the unappended bare body is a large component of the total drag. However, this study is not an all encompassing study to determine the reliability of RANS codes for drag prediction. Rather, a series of calculations are performed for bodies of differing length/diameter ratios corresponding to the data obtained by Gertler ¹ for Reynolds numbers in the range 2.0×10^6 to 25.0×10^6 . Four different grids are used for the calculations to give an indication of how drag predictions can be affected by different grids. The RANS code used for the present calculations is the axisymmetric version of the David Taylor Navier-Stokes (DTNS) ^{2, 3} code developed at CDNSWC.

SOLUTION TECHNIQUE

The steady incompressible Reynolds averaged Navier-Stokes equations are solved using the axisymmetric version of the DTNS code. The DTNS codes were developed

by Gorski^{2,3} and have since been applied to a variety of submarine^{4,5} (including body forces for propulsion modeling⁶) and ship^{7,8} configurations including transom sterns⁹. Other work with the DTNS codes was aimed at extending their applicability by introducing more physics with the inclusion of stratification¹⁰. In addition, because of their accuracy and applicability to complex configurations, the DTNS codes have been used as a turbulence modeling testbed by Gorski^{11,12} and at the NASA Lewis Research Center by Steffan^{13,14}. A brief description of the DTNS flow solver will now be given.

The DTNS codes use the pseudo-compressibility approach where an artificial time term is added to the continuity equation and then all of the equations are marched in time. The solver is based on a cell centered finite volume formulation where the dependent variables are stored at cell centers and the "fluxes" are computed across the cell faces. The Navier-Stokes equations contain first derivative convective terms and second derivative viscous terms. The viscous terms are numerically well-behaved diffusion terms and are discretized using standard central differences. The convective terms are treated using Roe's¹⁵ approximate Riemann solver. A Jacobian matrix is formed for each of the convective flux terms for which eigenvectors and eigenvalues are obtained. By differencing these flux terms based on the sign of their eigenvalues stability can be achieved without any artificial dissipation terms being added to the equations. For the present calculations a third-order upwind biased discretization is used for the convective terms. More details of how this discretization method is applied to the Navier-Stokes equations for incompressible flows were presented by Gorski².

The equations are solved in an implicit coupled manner using a first-order accurate upwind scheme for the convective terms and standard central differences for the viscous terms. The implicit treatment of the viscous terms adds more numerical stability to the solution. This creates a diagonally dominant system which requires the inversion of block tri-diagonal matrices. The implicit side of the equations are only first order accurate because of the treatment for the convective terms, but the final converged solution has the high order accuracy of the explicit part of the equations. Additionally, a spatially varying time step based on the local eigenvalues is used for faster convergence rates. However, discontinuities in the grid and extremely tight clusterings can significantly impact the stability and convergence rate of any numerical method, this one included.

For the present calculations the algebraic eddy viscosity model of Baldwin and Lomax¹⁶ is used. All of the grids used are O-type grids which wrap around the leading and trailing edges of the bodies. Consequently, no treatment is included for the wake region downstream of the bodies of revolution.

NUMERICAL RESULTS

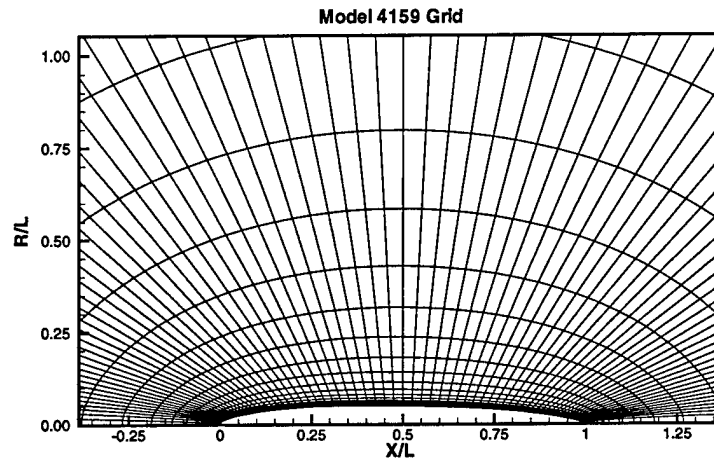
The calculations correspond to a series of mathematically related streamlined bodies of revolution, designated as Series 58, which are derived from a sixth degree polynomial.

A number of these bodies with varying length to diameter ratios and various leading and trailing edge radii were tested by Gertler ¹ specifically for resistance purposes. The models were all 9 feet (2.74 m) long and tested in the David Taylor Model Basin. For towing purposes two struts were attached to each model. Due to interference between the models and the towing struts the measured resistance is higher than on the bare bodies themselves. Consequently, a pair of dummy struts, similar to the towing struts, were also constructed and mounted at ninety degrees to the original struts. Tests were conducted with and without the dummy struts with the difference giving an estimate of strut-interference effects. This strut-interference value can then be subtracted from the resistance obtained for the body of revolution with towing struts to obtain an estimate of the resistance of the body of revolution alone. Different values of strut-interference coefficient are obtained for the different models, but it is assumed the value for each individual model is independent of Reynolds number. The experimental data as presented here has the strut-interference coefficient removed for comparison with the bare body calculations. The experimental measurements were conducted both with smooth models and with a 1/2 inch (1.27 cm) sand strip placed at $X/L = 0.05$ to better stimulate transition to turbulence. The models were towed at a depth of 9 feet (2.74 m) which was thought to minimize free surface effects.

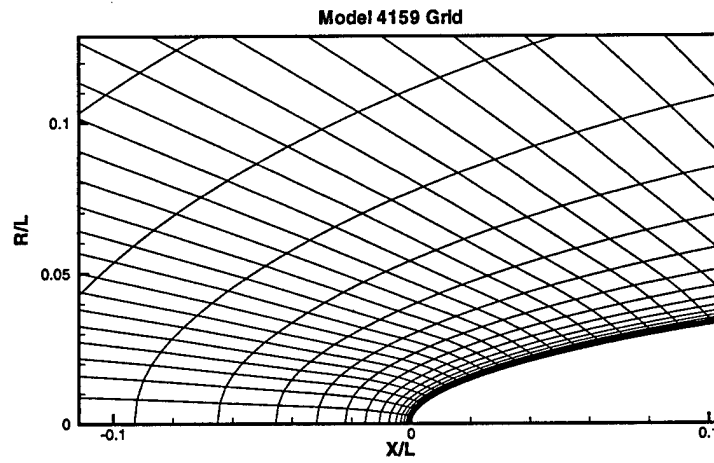
Calculations are presented for a range of Reynolds numbers ranging from 2.0×10^6 to 25.0×10^6 , based on body length, which covers the range over which the experiments were performed. No attempt is made to model transition in the calculations and all computations are done as if the bodies are fully turbulent. The models computed are 4159, 4158, and 4155 corresponding to length to diameter ratios of 10, 8, and 5, respectively.

Model 4159

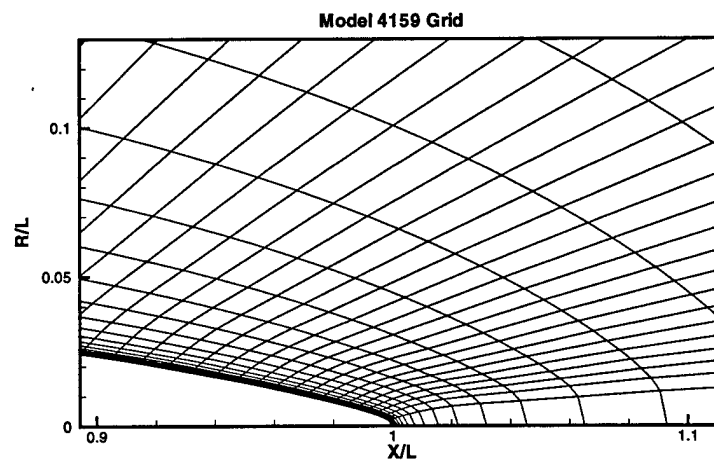
Model 4159 has a length to diameter ratio of 10 with a wetted surface area of 19.64 square feet (1.82 m²). Calculations are performed on four different grids. Two coarse grids, designated C0 and C1, have 81 points along the body and 41 points going from the body out to the outer boundary of the computational domain which extends to about five body lengths from the body. Grid C0, with details of the grid near the leading and trailing edges, is shown in Fig. 1. Grid C1 has the same number of points and the same distribution along the body. However, the C1 grid is more tightly clustered near the wall so that at the highest Reynolds number computed the centroid of the first point off of the wall is at $y^+ \approx 1$. This tight clustering will also put more grid points in the boundary layer. Two fine grids are also used, designated F0 and F1. Grid F0, with details of the grid near the leading and trailing edges, is shown in Fig. 2. These two fine grids have 161 points along the body and 81 points going from the body out to the outer boundary of the computational domain. As with the coarse grids F0 and F1 have the same point distribution along the body. Grid F1 is more tightly clustered normal to the body with the first centroid off of the wall at $y^+ \approx 1$ for the highest Reynolds



(a) Full grid.

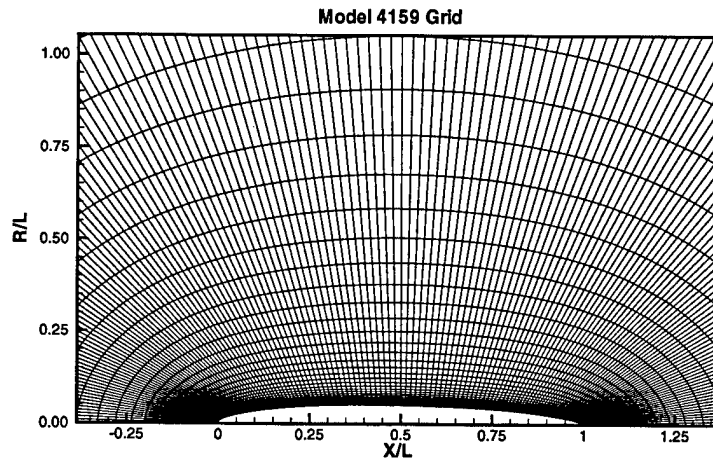


(b) Detail around the leading edge.

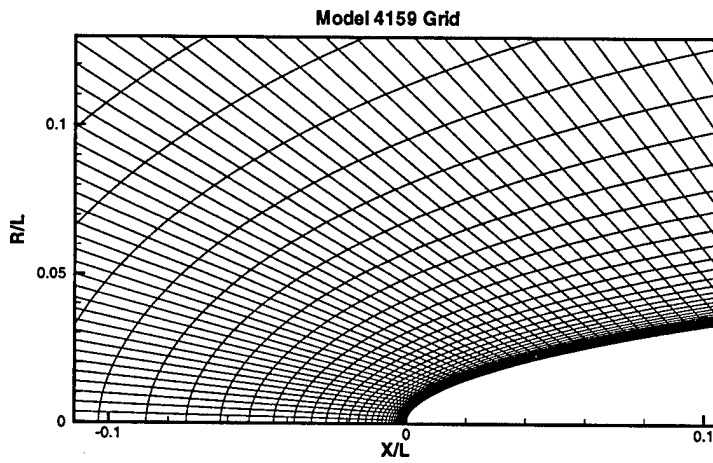


(c) Detail around the trailing edge.

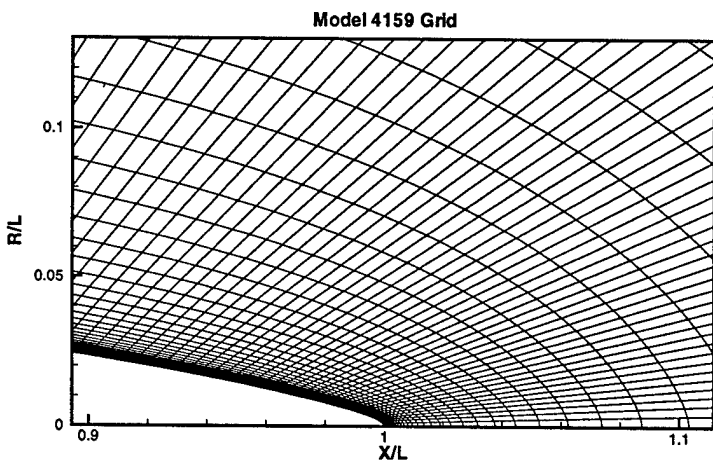
Fig. 1. Coarse grid for Model 4159.



(a) Full grid.



(b) Detail around the leading edge.



(c) Detail around the trailing edge.

Fig. 2. Fine grid for Model 4159.

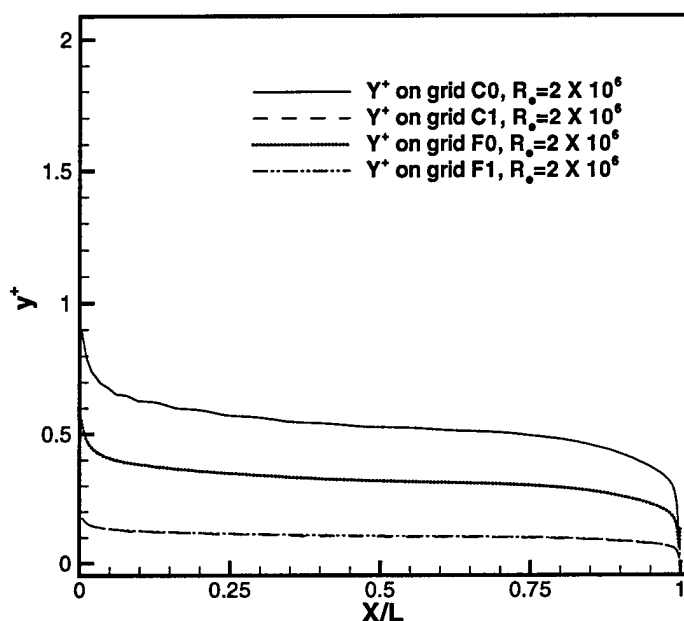


Fig. 3. Y^+ for Model 4159 at a Reynolds number of 2.0×10^6 .

number computed. All four grids are generated algebraically with surface normalcy imposed close to the body, particularly for the coarse grids C0 and C1. Grids C0 and C1 are generated independently from the F0 and F1 grids and are not obtained by removing every other point from them.

An indication of the differences in clustering between the grids can be obtained by observing the distance of the first centroid off of the wall in wall coordinates. Shown in Fig. 3 is the y^+ value of the first centroid off of the wall for the four grids at a Reynolds number of 2.0×10^6 . All are near y^+ of one or less, which should be more than adequate for skin friction calculations, with C1 and F1 very tightly clustered and nearly indistinguishable. Law of the wall plots for C0 and C1 show good comparison with the equation of Spalding¹⁷ at two locations near the midbody (Fig. 4). Grids F0 and F1, being finer than C0 and C1, reproduce Spalding's equation just as well. Spalding's¹⁷ formula, which uses the same constants as the Clauser fit, is a formula for the law of the wall which smoothly transitions from the inner layer, where the linear law applies, to the outer layer where the law of the wall equation applies.

At the higher Reynolds number of 25×10^6 the first centroid off of the wall for grids C0 and F0 is fairly far out in the viscous sublayer (Fig. 5) near y^+ values of approximately 7 and 4, respectively. The grids are not changed for the different Reynolds numbers. This becomes detrimental to the law of the wall prediction as shown in Fig. 6. Grids C1 and F1 still have the first centroid around y^+ of one and still provide a good comparison

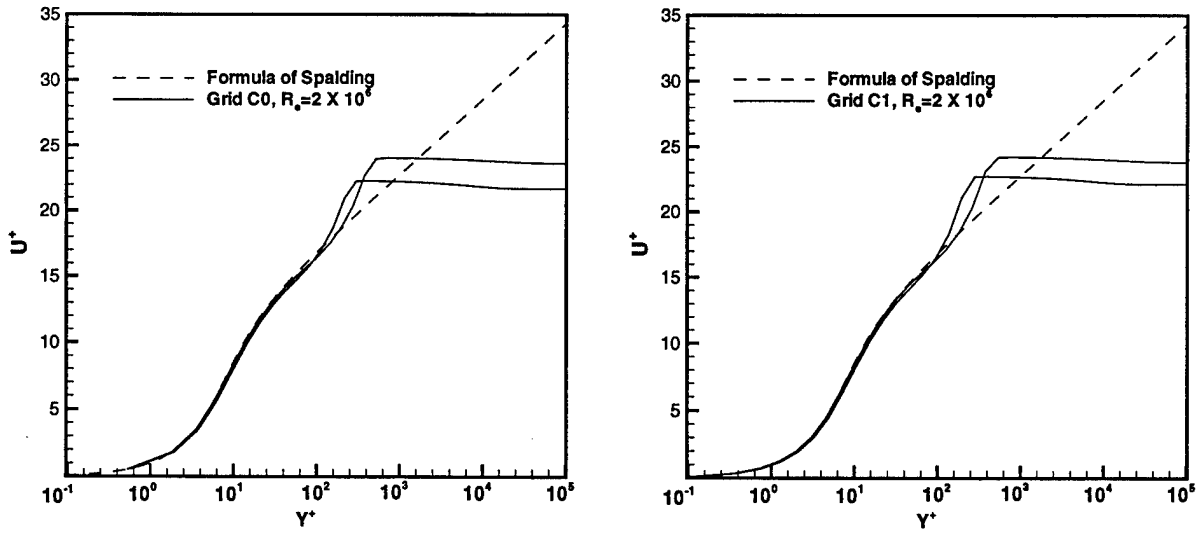


Fig. 4. Law of the wall plots at $R_e = 2.0 \times 10^6$.

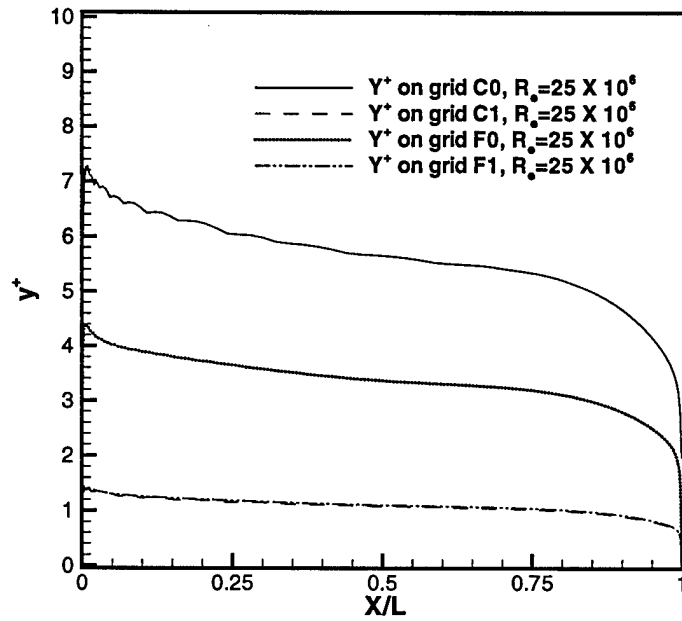


Fig. 5. Y^+ for Model 4159 at a Reynolds number of 25.0×10^6 .

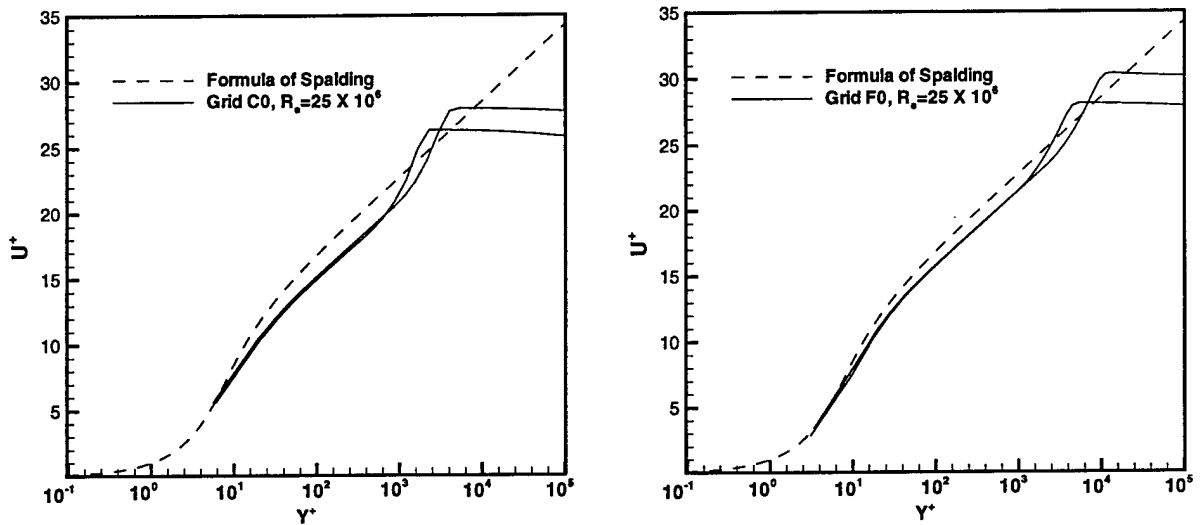


Fig. 6. Law of the wall plots for grids C0 and F0 at $R_e = 25.0 \times 10^6$.

with the law of the wall as shown in Fig. 7.

The predicted resistance coefficient, C_t , for a range of Reynolds numbers on all four grids is shown in Fig. 8 along with the experimental data of Gertler¹. Here the resistance coefficient is given by

$$C_t = \frac{\text{Resistance}}{1/2\rho S U^2}$$

where ρ is the density, S is the wetted surface area, and U is the free stream velocity. A constant value of 0.00042 has been subtracted from the data as originally published by Gertler to account for strut-interference. Two curves are included for the experimental data; one in which sand has been added to stimulate transition to turbulence and one where the body is smooth. The data with sand has a higher resistance coefficient than the smooth model for all Reynolds numbers tested. This indicates that there is an added resistance due to the sand even at the higher Reynolds numbers where it is not necessary to trip the flow for transition. Gertler has discussed this and devised a resistance coefficient due to the sand for the interested reader. The calculations on all four grids tend to agree with the values for the model with sand at the low Reynolds numbers. At the higher Reynolds numbers the two grids with the finer clustering, C1 and F1, tend to agree with the two data curves; C1 the data without sand and F1 the data with sand. Both F1 and C1 predictions remain parallel to each other and represent the trends of the data quite well. The two grids which are not as finely clustered, C0 and F0, tend to predict high values of resistance at the higher Reynolds numbers. It can also be seen that these predictions tend to rise with increasing Reynolds number and are not parallel to the experimental data. These results indicate that predicting

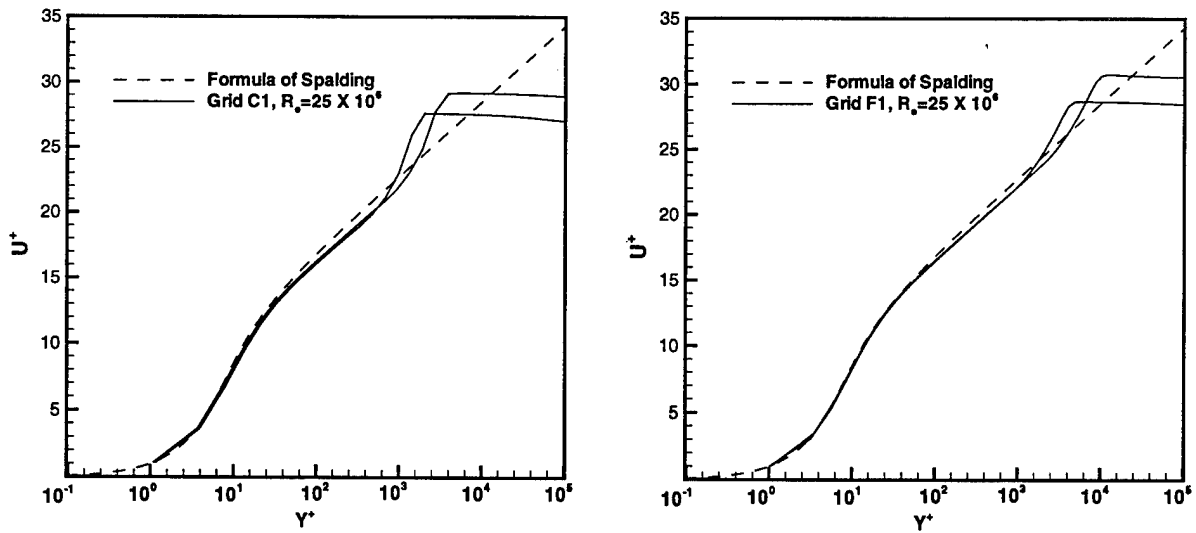


Fig. 7. Law of the wall plots for grids C1 and F1 at $R_e = 25.0 \times 10^6$.

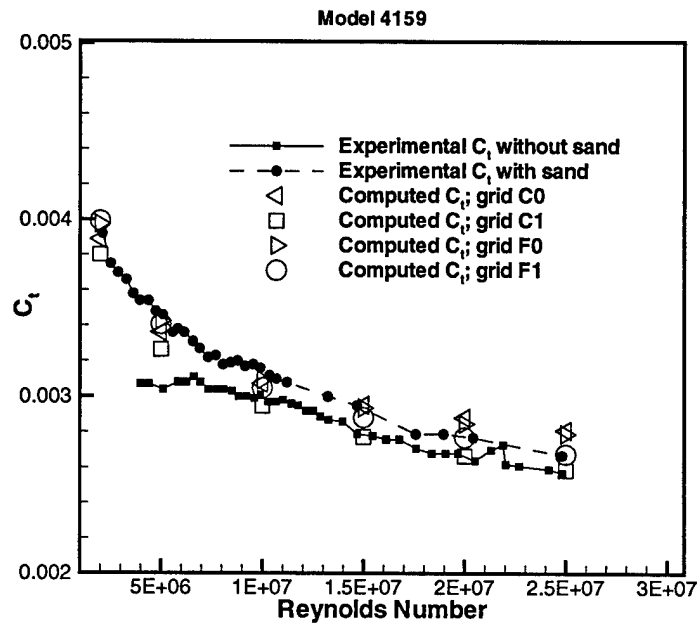


Fig. 8. C_f for Model 4159.

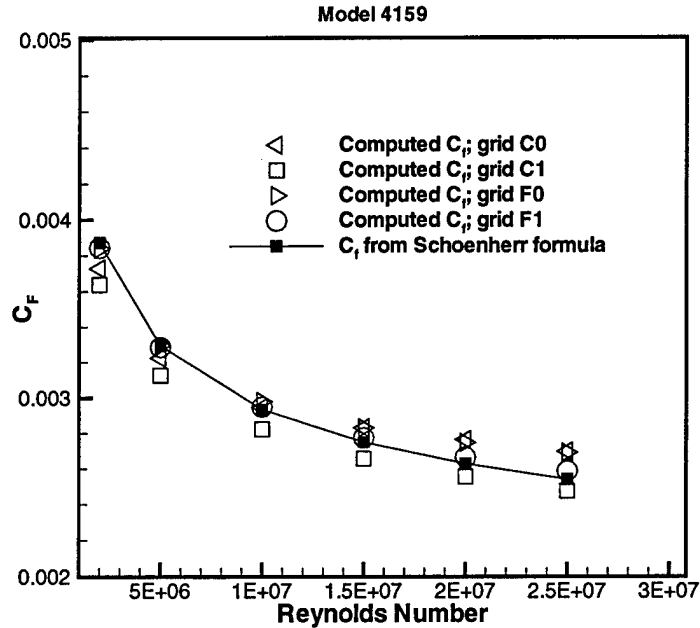


Fig. 9. C_F for Model 4159.

the correct resistance may be more a function of having adequate resolution of the boundary layer and first point off of the wall than a function of the actual number of grid points.

The resistance is obtained by integrating the pressure and viscous stresses over the hull. Intuitively, one would think that the frictional resistance would be controlled by the first point off of the wall and boundary layer resolution. A comparison of the frictional resistance coefficient, C_F , for the four grids is shown in Fig. 9 along with the values obtained from the Schoenherr formula

$$\frac{0.242}{\sqrt{C_F}} = \log_{10}(R_e \cdot C_F).$$

The RANS solution on grid F1 closely matches the Schoenherr formula and the solution on grid C1 is roughly parallel to it. One cannot say that F1 is better than C1 because of this since the Schoenherr formula is a generic formula and only has Reynolds number dependence and no body dependence. However, one can see that predictions with both grids have the same trend. Grids C0 and F0 do fine at the low Reynolds numbers, but their values rise at the higher Reynolds numbers repeating the trend seen for the total resistance coefficient. If we look at local skin friction for these four grids we see that at the low Reynolds number of 2.0×10^6 much the same skin friction is obtained (Fig. 10). However, the small differences seen lead to noticeable differences when they are integrated for the total resistance. Small differences in grid normalcy and spacing

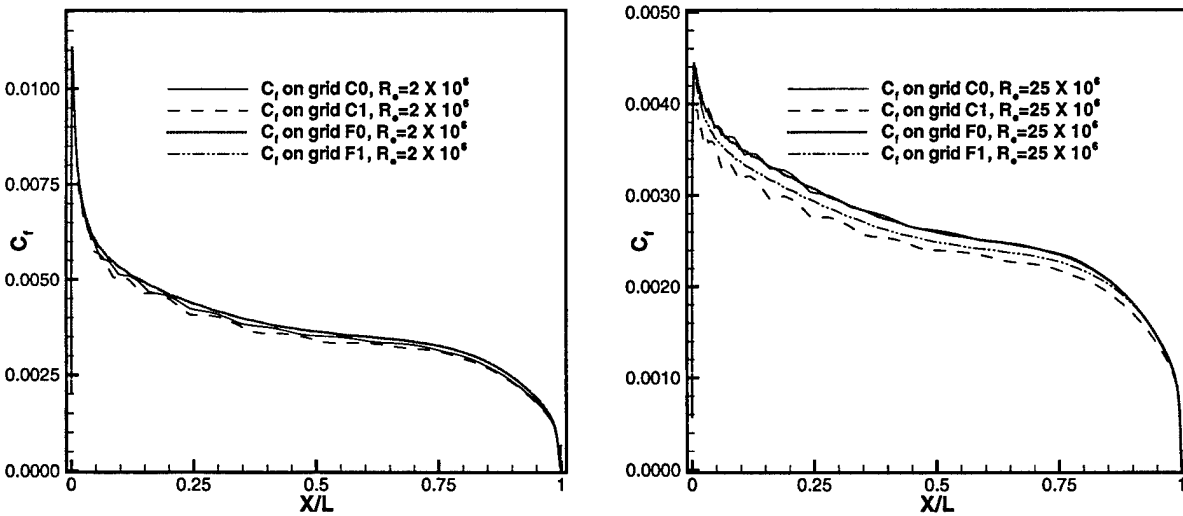


Fig. 10. Skin friction comparisons for Model 4159.

lead to these small differences in the local skin friction. The use of the Baldwin-Lomax turbulence model for the present computations may have highlighted these grid differences somewhat since the Baldwin-Lomax model relies on a computed length scale which can be highly grid dependent. At the low Reynolds numbers grids F0 and F1 give nearly identical results for skin friction while grids C0 and C1 produce slightly lower values. For the higher Reynolds numbers the differences in local skin friction become more apparent. Here grids C0 and F0 tend to predict higher values than grids C1 and F1 which leads to the overprediction of total and frictional resistance on grids C0 and F0.

The residual resistance coefficient, C_r is obtained from

$$C_r = C_t - C_F$$

and is basically the resistance due to pressure forces on the body. The residual resistance for the four grids is shown in Fig. 11 along with the experimental data of Gertler. For the experimental data the residual resistance has been obtained by subtracting the frictional resistance obtained with the Schoenherr formula from the total resistance. Again the experimental data with and without sand are shown. It can be seen that below a Reynolds number of approximately 1.0×10^7 the data without sand is negative. This indicates laminar flow over part of the body since the residual resistance is obtained by subtracting the turbulent frictional resistance from the total resistance. It is postulated by Gertler that the small hump in the experimental curves around a Reynolds number of 1.0×10^7 is due to free surface effects which decrease at the higher Reynolds numbers. The computed values are all close to each other which is not surprising since the computed

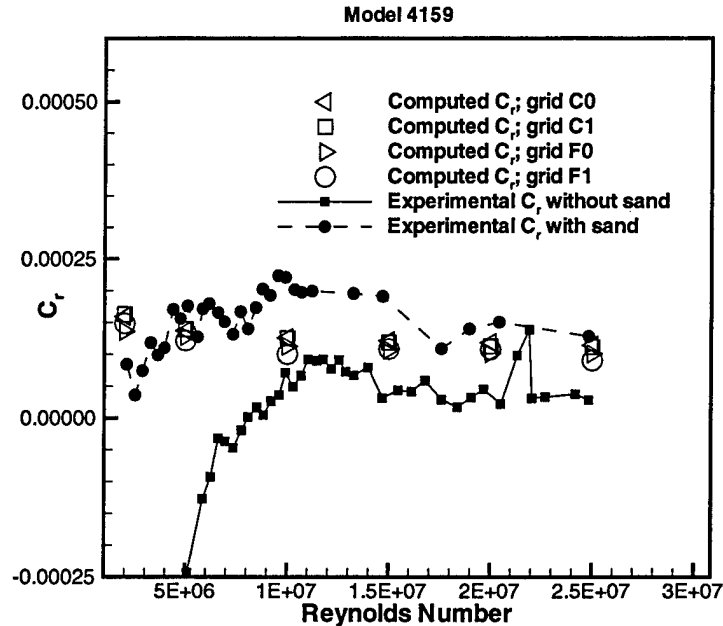


Fig. 11. C_r for Model 4159.

pressure distributions are nearly identical between the four grids as shown in Fig. 12. The computed C_r tends toward a constant value at the higher Reynolds numbers which is the expected behavior. It can be seen that there is some difference between the C and F grids with the C grids giving slightly higher C_r values than the F grids. It would appear from this that the number of points wrapping around the body does have some impact on the residual resistance prediction. However, considering the large difference in leading and trailing edge resolution of the grids the predicted difference in C_r does not seem to be significant for Model 4159 predictions.

Model 4158

Model 4158 has a length to diameter ratio of 8 with a wetted surface area of 24.58 square feet (2.28 m²). Again calculations are performed on four different grids with much the same point distributions as for model 4159. The coarse, C0, and fine, F0, grids are shown in Figs. 13 and 14. Law of the wall and y^+ plots are very nearly identical to those shown earlier for Model 4159 so are not repeated here. The same trends as Model 4159 between the predictions on the four grids and the experimental data are seen in the comparisons of total and frictional resistance, Figs. 15 and 16, respectively.

Here a strut-interference coefficient of 0.00040 has been subtracted from the data of Gertler. The total resistance predicted with grids C1 and F1 are roughly parallel to each other and very nearly straddle the experimental data. The resistance predicted with grids C0 and F0 tends to rise with Reynolds number apparently due to insufficient

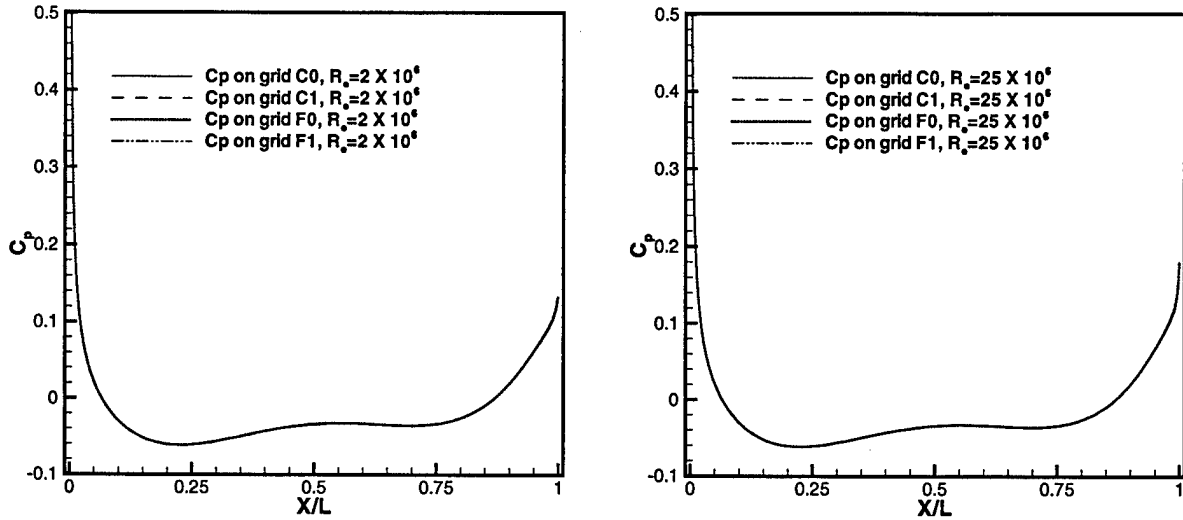
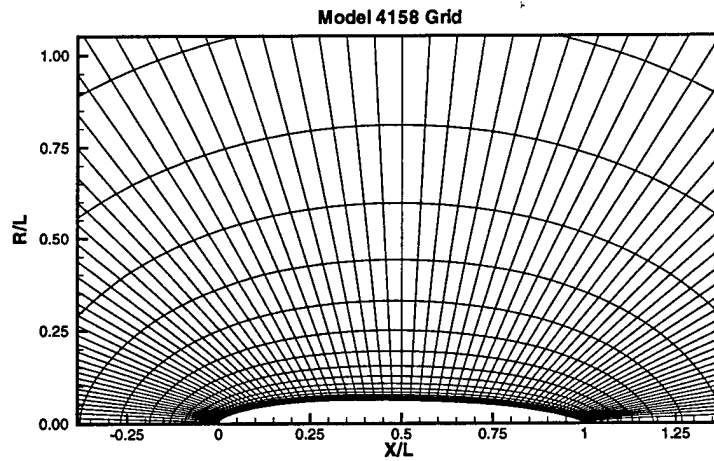


Fig. 12. Surface pressure comparison for Model 4159.

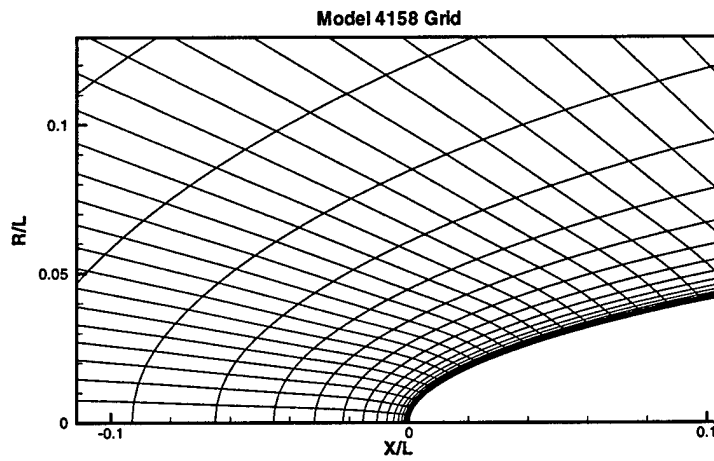
resolution near the wall. The predicted local skin friction at the low Reynolds numbers is similar between the four grids (Fig. 17), but different enough to provide different integrated values of resistance. At the higher Reynolds numbers we again see grids C0 and F0 predicting higher levels of local skin friction than that computed on grids C1 and F1. It is important to note that differences in local skin friction might often be considered small when comparing computations and experiments, but these small differences accumulate when one integrates over the entire body for a force or moment prediction. For the residual resistance (Fig. 18) the experimental data again suggests a transition region for the case without the sand. The predicted values again asymptote to a constant value at higher Reynolds numbers, but here there is slightly more distinction between the values obtained on the coarse, or C grids, and those obtained on the F grids. Again there is little discernable difference between the surface pressure plots (Fig. 19).

Model 4155

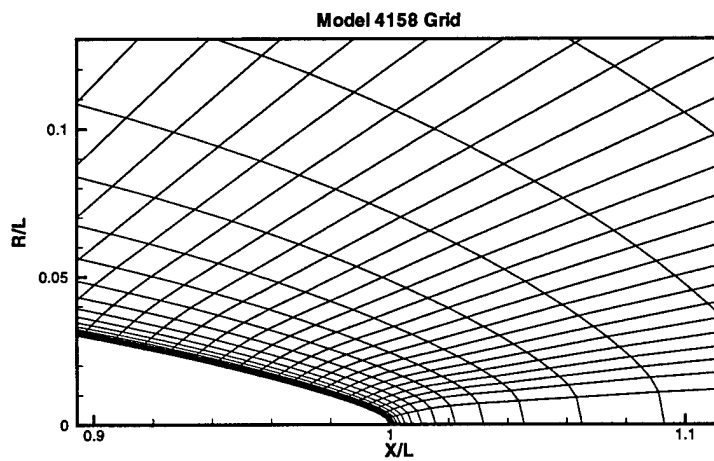
Model 4155 has a length to diameter ratio of 5 with a wetted surface area of 39.75 square feet (3.69 m²). Consequently it is much blunter than the previous geometries. Again calculations are performed on four different grids with much the same point distributions as for models 4159 and 4158. The coarse, C0, and fine, F0, grids are shown in Figs. 20 and 21. Despite the blunter nose of this geometry the law of the wall and y^+ plots are much the same as those shown earlier for Model 4159 so are not repeated here. The same trends between the predictions with the four grids and the experimental data are also seen in the comparisons of total and frictional resistance, Figs. 22 and 23,



(a) Full grid.

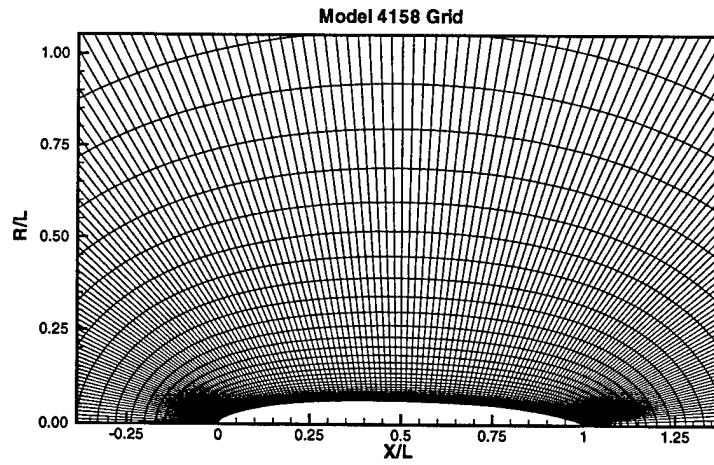


(b) Detail around the leading edge.

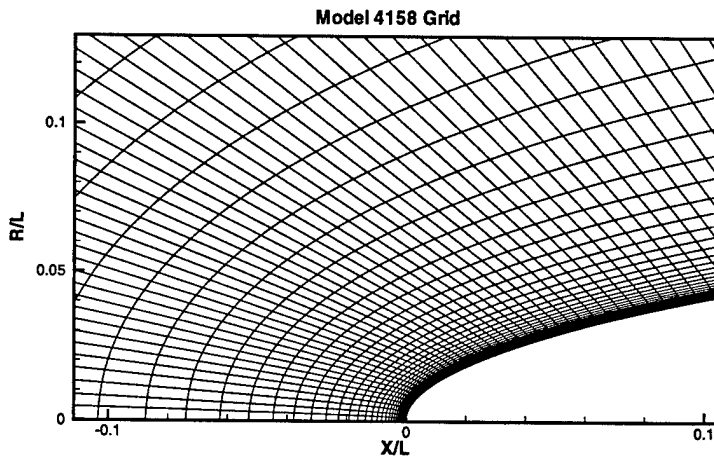


(c) Detail around the trailing edge.

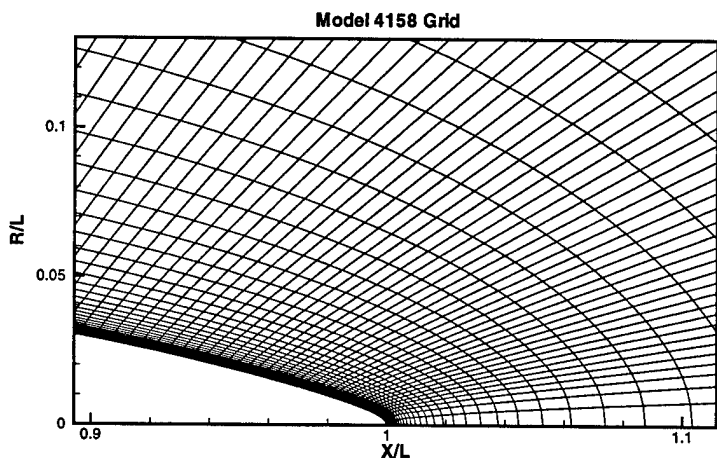
Fig. 13. Coarse grid for Model 4158.



(a) Full grid.



(b) Detail around the leading edge.



(c) Detail around the trailing edge.

Fig. 14. Fine grid for Model 4158.

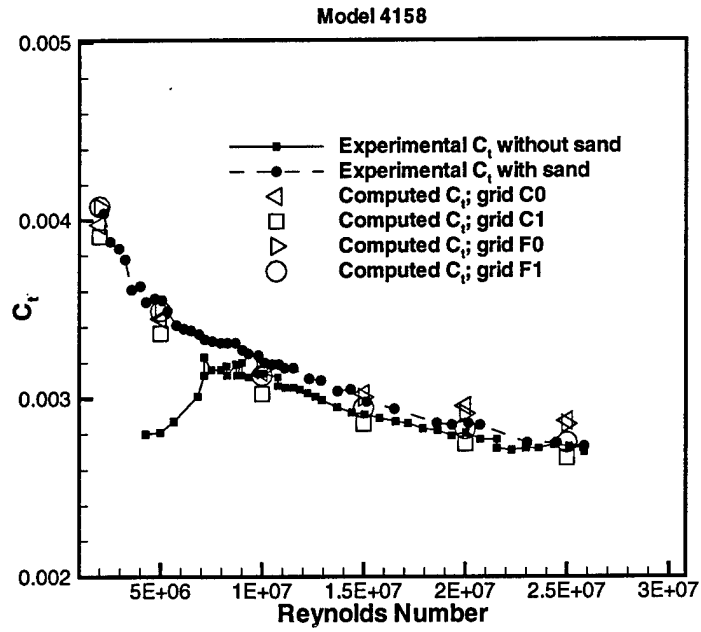


Fig. 15. C_t for Model 4158.

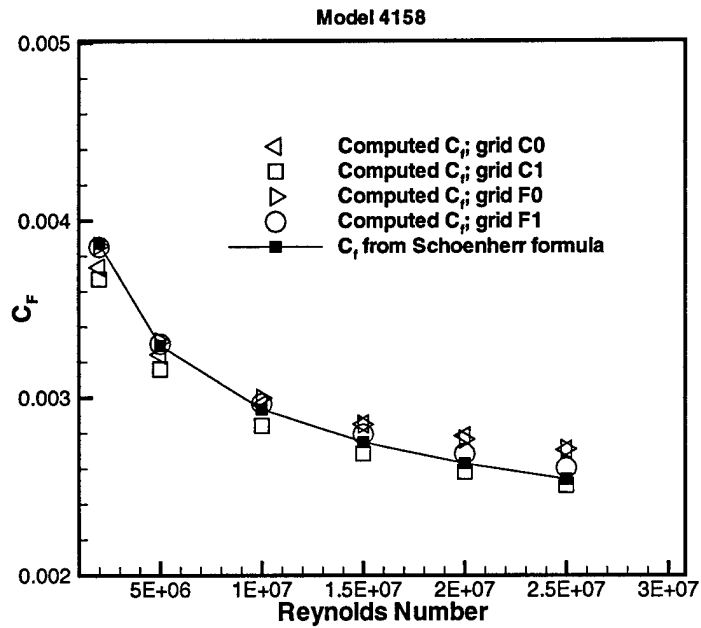


Fig. 16. C_f for Model 4158.

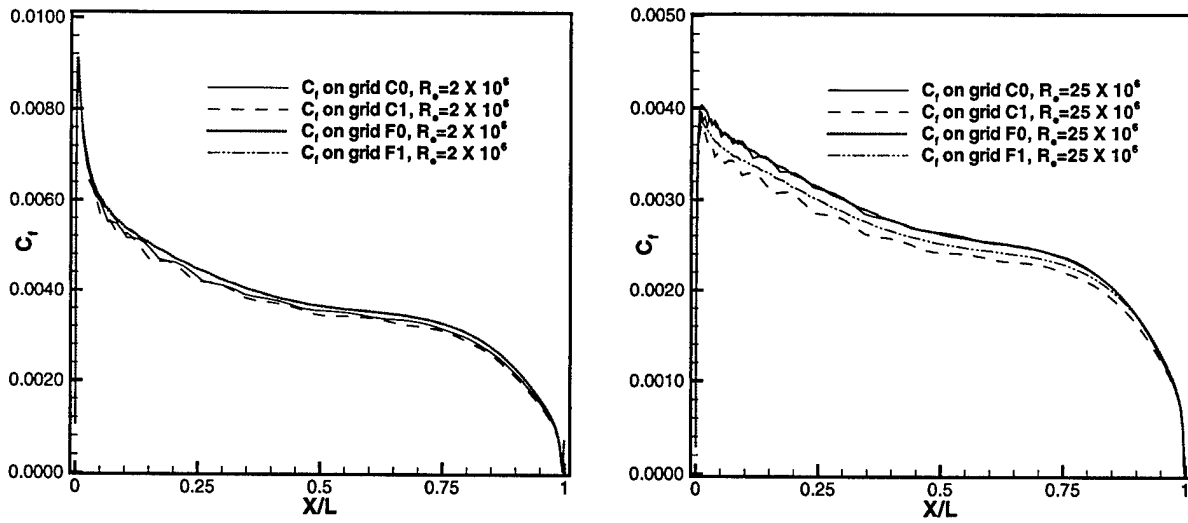


Fig. 17. Skin friction comparison for Model 4158.

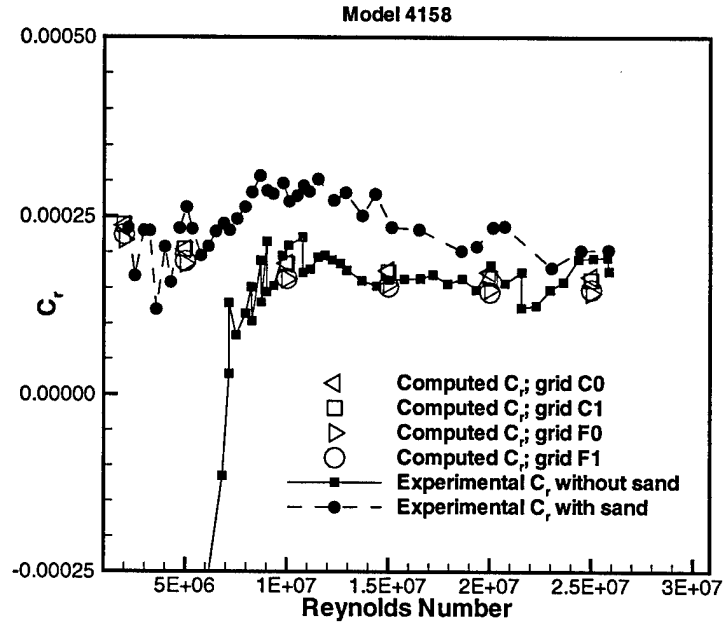


Fig. 18. C_f for Model 4158.

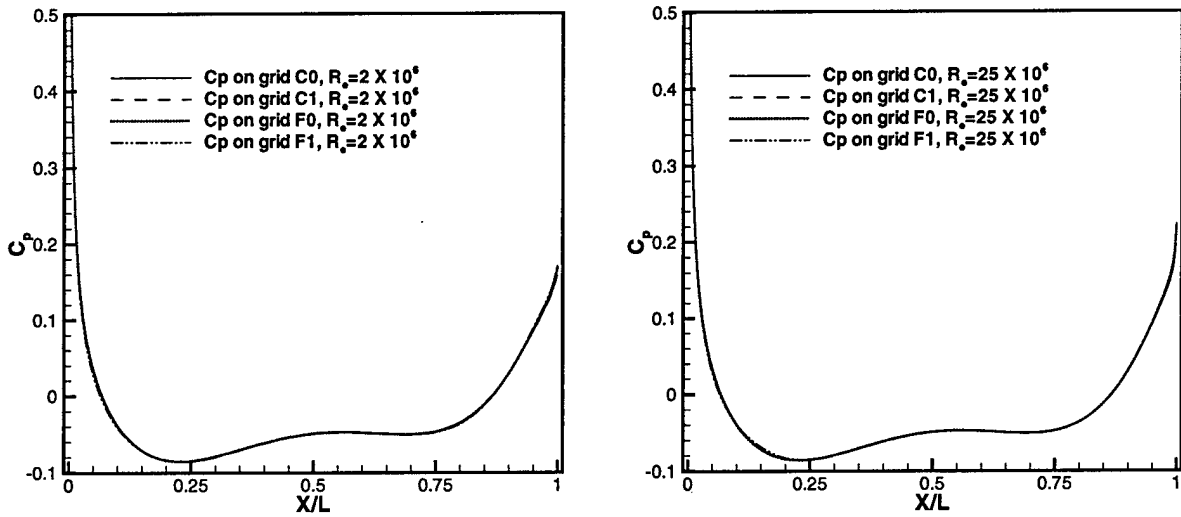
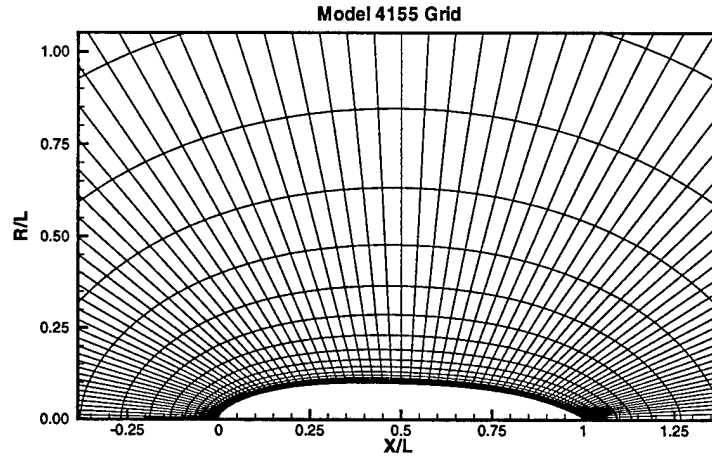
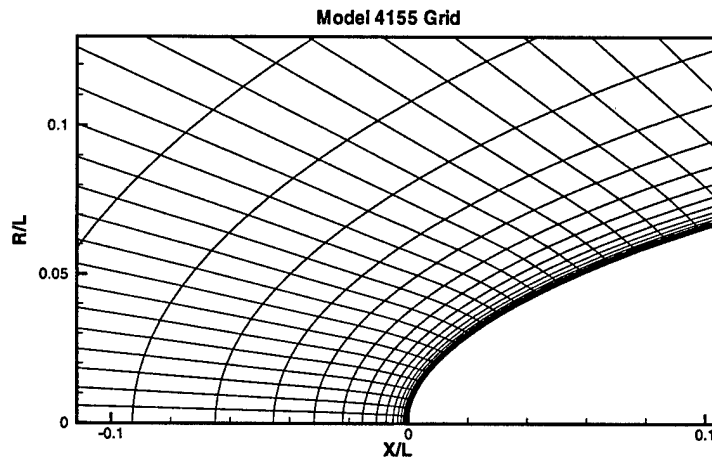


Fig. 19. Surface pressure comparison for Model 4158.

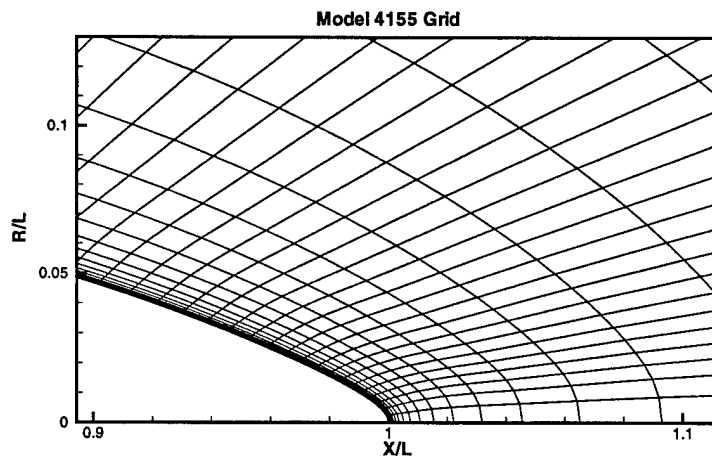
respectively. Here a strut-interference coefficient of 0.00035 has been subtracted from the experimental data of Gertler. Again, the total resistance predicted with grids C1 and F1 are roughly parallel to each other and match the trends of the experimental data well. The F1 prediction is consistently higher than the C1 prediction as seen earlier. At the low Reynolds numbers the experimental data with the sand is always predicted, but at the higher Reynolds numbers the predictions are somewhat between the two sets of experimental data. The resistance predicted with grids C0 and F0 tend to rise with Reynolds number apparently due to insufficient resolution right near the wall. It is interesting to note that the frictional resistance, Fig. 23, predicted with the Schoenherr formula is once again near the values predicted with the RANS code. Remember the Schoenherr curve is the same for all three models. There are some differences between the computed values and Schoenherr values for the different models, which can be seen from the different figures, but overall the Schoenherr formula seems to give a reasonably good estimate of the frictional resistance for this series of models as compared to RANS calculations. The local skin friction at the low Reynolds number of 2.0×10^6 has more differences between the four grids than seen earlier (Fig. 24). At the low Reynolds number grids F1 and F0 give nearly identical results. The differences between the C and F grids is believed to be due to surface normalcy and other detailed differences between the grids. At the high Reynolds number of 25.0×10^6 grids C0 and F0 again predict higher levels of local skin friction than that computed on grids C1 and F1. For the residual resistance, Fig. 25, the experimental data again suggests a transition region without the sand. There is also a much larger hump region in the experimental data than seen previously which is thought to be due to free surface effects. The predicted



(a) Full grid.

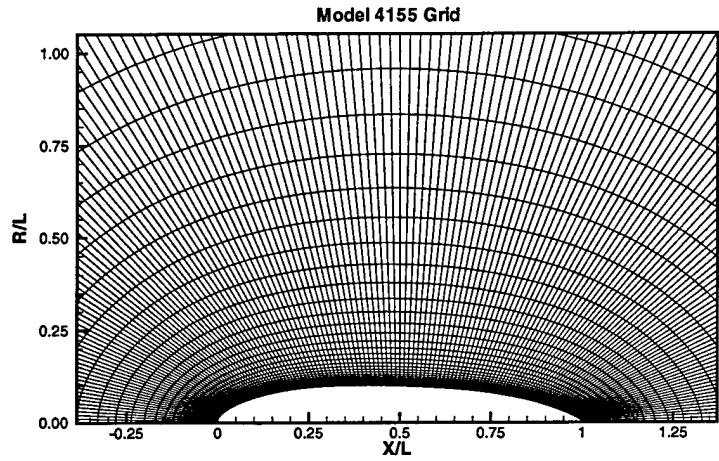


(b) Detail around the leading edge.

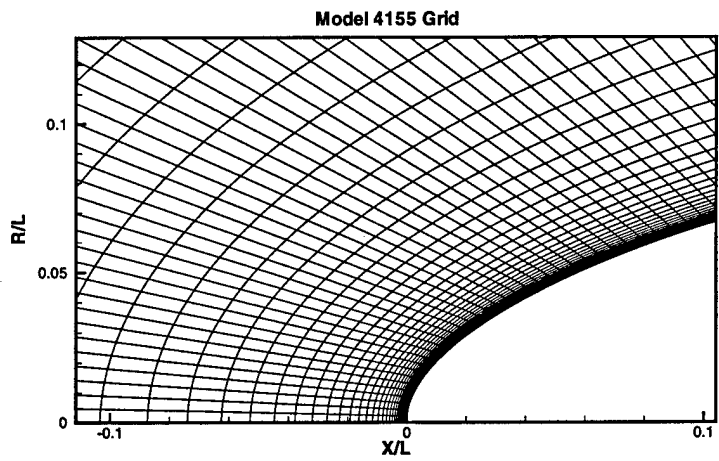


(c) Detail around the trailing edge.

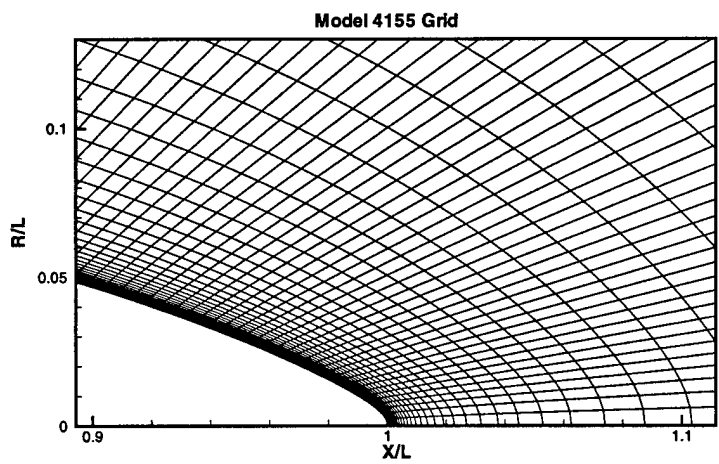
Fig. 20. Coarse grid for Model 4155.



(a) Full grid.



(b) Detail around the leading edge.



(c) Detail around the trailing edge.

Fig. 21. Fine grid for Model 4155.

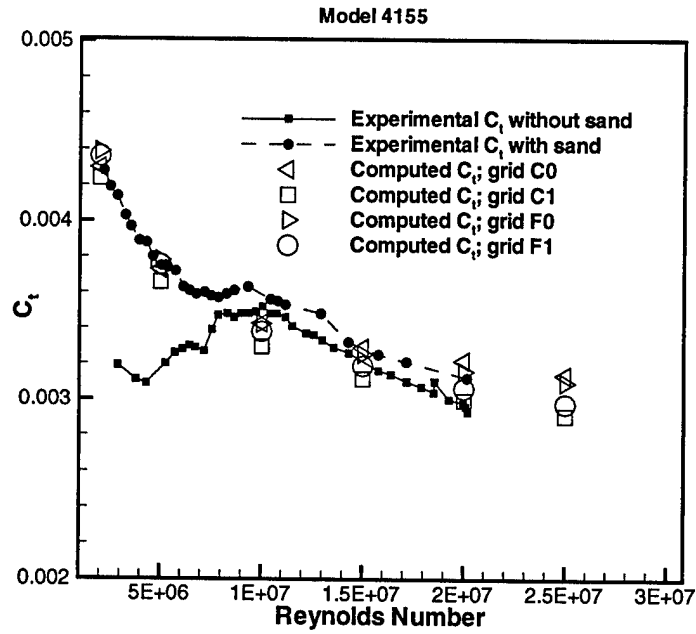


Fig. 22. C_t for Model 4155.

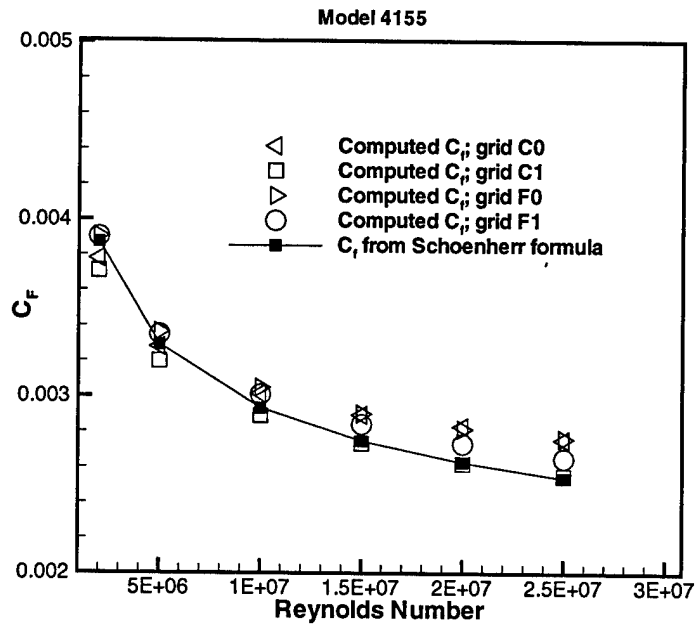


Fig. 23. C_f for Model 4155.

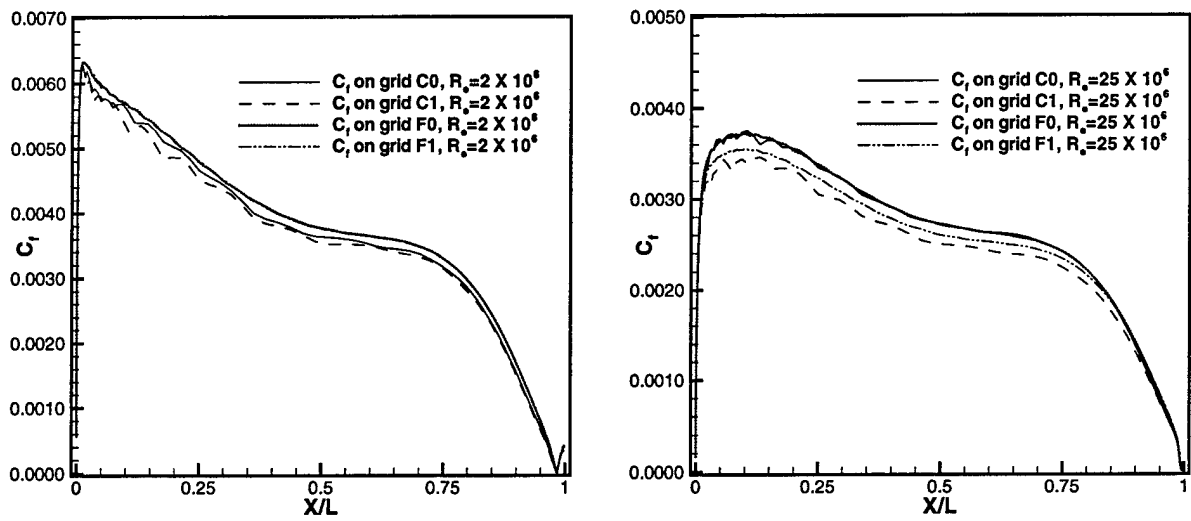


Fig. 24. Skin friction comparison for Model 4155.

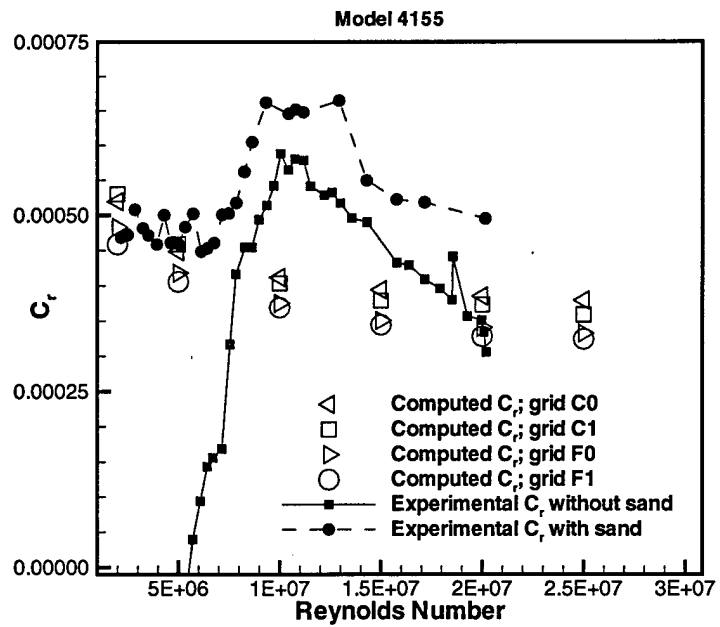


Fig. 25. C_d for Model 4155.

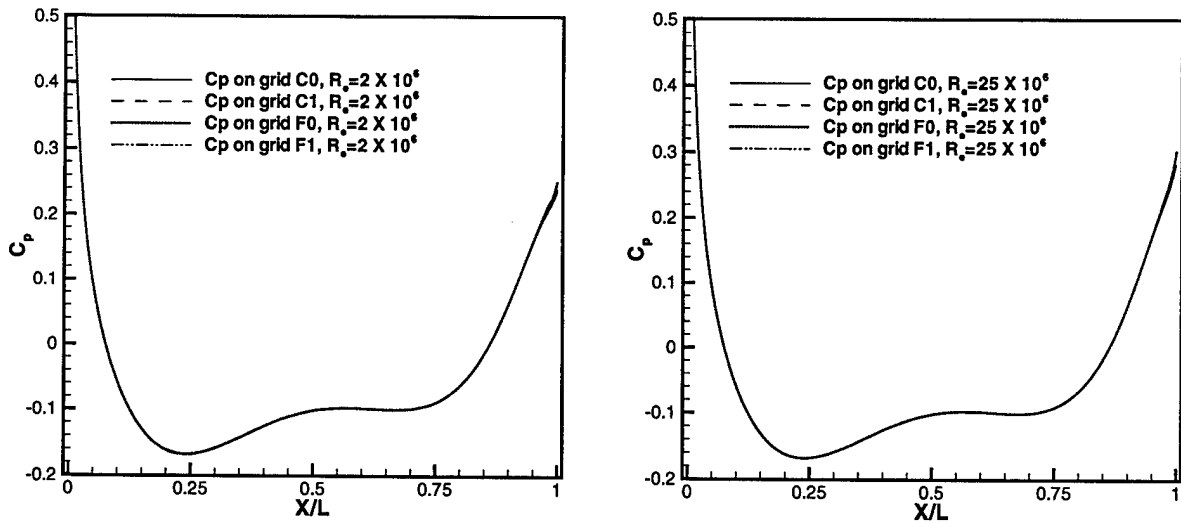


Fig. 26. Surface pressure comparison for Model 4155.

values are again asymptoting to a constant value at higher Reynolds numbers, but here there is more spread in the calculations than seen with the thinner bodies. Again there is a difference between the coarse and fine grid predictions indicating that at least for blunter bodies the number of points used to resolve the geometry does affect the residual/pressure resistance. It is interesting to note that the various grids seem to each be asymptoting to their own individual value of C_r at high Reynolds numbers. Unlike the previous surface pressure predictions, for this model there are some small differences near the trailing edge as shown in Fig. 26.

CONCLUSIONS

As already mentioned RANS computations are being more routinely carried out for fully appended ship and submarine configurations. These computations are being used to provide force and moment estimates. The intent of this work is to determine how reliably such RANS computations can provide drag estimates for unappended bodies of revolution. Calculations are demonstrated for three different bodies with length/diameter ratios of 10, 8, and 5 over a range of Reynolds numbers from 2.0×10^6 to 25.0×10^6 , based on body length. Grid resolutions are typical of what is currently used to grid the hull of a fully appended ship or submarine configuration. In general as long as the first point off of the wall is sufficiently close the computations agree with the total resistance, as experimentally measured by Gertler¹, quite well. At low Reynolds numbers the experimental flow was transitional and the computations agree with the model data with sand present. At higher Reynolds numbers the predictions on grids C1 and F1, whose first point off of the wall is always at $y^+ \approx 1$ or less, are within

the differences seen in the experimental data between the cases with and without sand present on the model. If the first point off of the wall is too far away, as for grids C0 and F0, the predicted resistance tends to be too high. This is regardless of the number of grid points used for the calculation. It seems the actual number of points on or normal to the body is not as significant as the distance of the first point off of the wall for these calculations.

The pressure or residual resistance is computed quite well with all of the grids with the calculations generally falling between the experimental data with and without sand present at the higher Reynolds numbers. Again at the lower Reynolds numbers the calculations tended toward the experimental data with sand present. The values for C_r tend to asymptote to a constant value at higher Reynolds numbers. For the thinner bodies, with length to diameter ratios of 10 and 8, the number of points on the body does not significantly affect the solution. However, there is more of an affect for the bluntest body (length to diameter ratio of 5) with the finer grids providing a lower value than the coarser grids. The residual resistance seems to depend more on the number of points, or resolution of the body, than the distance of the first point off of the wall.

From these calculations it would definitely seem that RANS calculations can predict the correct resistance trends for axisymmetric bare bodies over a range of Reynolds numbers as long as the grid is sufficiently fine. Here the grids are not changed for the different Reynolds number calculations. The tightly clustered grids, C1 and F1, are probably too tightly clustered for low Reynolds number cases and the less clustered grids, C0 and F0, are not clustered enough for the high Reynolds number cases. From these calculations it appears that the best approach, for maintaining accuracy, is to regrid for different Reynolds numbers maintaining the first grid point off of the wall near a value of $y^+ \approx 1$. This value can be different for various RANS codes as different codes may have other accuracies and near wall treatments which would affect this value. However, a comparison of how well the law of the wall and viscous sublayer region is reproduced can give an indication of how much reliance can be put on a given calculation.

ACKNOWLEDGMENTS

The author would like to thank Mr. Alan Becnel for his help in obtaining the experimental data. In addition, this work was supported in part by grants of computer time from the U.S. Navy Hydrodynamic/Hydroacoustics Technology Center and the DoD HPC Center at the Naval Research Laboratory.

THIS PAGE INTENTIONALLY LEFT BLANK

REFERENCES

1. Gertler, M., "Resistance Experiments on a Systematic Series of Streamlined Bodies of Revolution - For Application to the Design of High-Speed Submarines," The David Taylor Model Basin, Report C-297, (April 1950).
2. Gorski, J. J., "TVD Solutions of the Incompressible Navier-Stokes Equations With an Implicit Multigrid Scheme," AIAA Paper No. 88-3699, *Proc. AIAA/ASME/SIAM/APS/ 1st Nat. Fluid Dynamics Cong.* 1:394-401 (1988).
3. Gorski, J. J., "Solutions of the Incompressible Navier-Stokes Equations Using an Upwind-Differenced TVD Scheme," *Lecture Notes in Physics*, 323:278-282 (1988).
4. Gorski, J. J., R. M. Coleman, and H. J. Haussling, "Computation of Incompressible Flow Around DARPA SUBOFF Bodies," DTRC Report No. 90/016, (June 1990).
5. Mautner, T. S., "Incompressible Euler Calculations About a Marine Vehicle With Fins and Stator Blades," AIAA Paper No. 92-3381, (1992).
6. Dai, C.M.H., J. J. Gorski, and H. J. Haussling, "Computation of an Integrated Ducted Propulsor/Stern Performance in Axisymmetric Flow", presented at SNAME Propulsors '91, (1991).
7. Gorski, J. J., R. M. Coleman, and H. J. Haussling, "Reynolds-Averaged Navier-Stokes Calculations of the Flow Around Two Ship Models," *Proc. SSPA-CTH-IIHR Workshop on Ship Viscous Flow*, Gothenburg, Sweden, (Sept., 1990).
8. Haussling, H. J. and J. J. Gorski, "Computation of Contaminated Nonlinear Free-Surface Flow about a Series 60 Hull," CARDIVNSWC-TR-95/037, (Dec. 1995)
9. Haussling, H. J., R. W. Miller and R. M. Coleman, "Computation of High-Speed Turbulent Flow About a Ship Model with a Transom Stern," CRDKNSWC/HD-0200-51, (Sept. 1997).
10. Slomski, J. F. and J. J. Gorski, "Fluid Stratification at a Free Surface Induced by a Rising Vortex Pair," AIAA Paper No. 96-1956, (1996)
11. Gorski, J. J., "Application of Vorticity Transport Analysis to the Development of Physically Accurate Turbulent Models," Ph.D. Dissertation, University of Maryland, College Park, Maryland (1993).
12. Gorski, J. J. and P. S. Bernard, "Vorticity Transport Analysis of Turbulent Flows," *J. of Fluids Eng*, 117:410-416, (Sept. 1995).
13. Steffen, C. J., "An Investigation of DTNS2D for Use as an Incompressible Turbulence Modelling Test-bed," NASA TM 105593, (March, 1992).

14. Steffen, C. J., "A Critical Comparison of Several Low Reynolds Number $k - \epsilon$ Turbulence Models for Flow Over a Backward Facing Step," AIAA Paper No. 93-1927, (1993).
15. Roe, P. L., "Approximate Riemann Solvers, Parameter Vectors, and Difference Schemes," *J. of Comp. Physics*, 43:357-372 (1981).
16. Baldwin, B. S. and H. Lomax, "Thin Layer Approximation and Algebraic Model for Separated Turbulent Flows," AIAA Paper No. 78-257, (1978).
17. Spalding, D. B., "A Single Formula for the Law of the Wall," *J. of App. Mechs.*, 455-457 (Sept. 1961).